ACS APPLIED MATERIALS & INTERFACES

Research Article

www.acsami.org

Self-Arranged Misfit Dislocation Network Formation upon Strain Release in $La_{0.7}Sr_{0.3}MnO_3/LaAlO_3(100)$ Epitaxial Films under Compressive Strain

José Santiso,[*,†] Jaume Roqueta,[†] Núria Bagués,[†,‡] Carlos Frontera,[‡] Zorica Konstantinovic,[⊥] Qiyang Lu,[§] Bilge Yildiz,[§] Benjamín Martínez,[‡] Alberto Pomar,[‡] Lluis Balcells,[‡] and Felip Sandiumenge[‡]

[†]Catalan Institute of Nanoscience and Nanotechnology (ICN2), CSIC, and the Barcelona Institute of Science and Technology (BIST), Campus UAB, Bellaterra, Barcelona 08193, Spain

[‡]Materials Science Institute of Barcelona (ICMAB), CSIC, Campus UAB, Bellaterra, Barcelona 08193, Spain

[§]Massachusetts Institute of Technology (MIT), Cambridge, Massachusetts 02139, United States

[⊥]Center for Solid State Physics and New Materials, Institute of Physics Belgrade, University of Belgrade, Pregrevica 118, 11080 Belgrade, Serbia

Supporting Information

ABSTRACT: Lattice-mismatched epitaxial films of $La_{0.7}Sr_{0.3}MnO_3$ (LSMO) on $LaAlO_3$ (001) substrates develop a crossed pattern of misfit dislocations above a critical thickness of 2.5 nm. Upon film thickness increases, the dislocation density progressively increases, and the dislocation spacing distribution becomes narrower. At a film thickness of 7.0 nm, the misfit dislocation density is close to the saturation for full relaxation. The misfit dislocation arrangement produces a 2D lateral periodic structure modulation ($\Lambda \approx 16$ nm) alternating two differentiated phases: one phase fully coherent with the substrate and a fully relaxed phase. This modulation is confined to the interface region between film and substrate. This phase separation is clearly identified by X-ray diffraction and further proven in the macroscopic resistivity measurements as a combination of two transition temperatures (with low and high T_c). Films thicker than 7.0 nm show progressive relaxation, and their macroscopic resistivity becomes similar than that of the bulk material. Therefore, this study identifies the growth conditions and thickness ranges that facilitate the formation of laterally modulated nanocomposites with functional properties notably different from those of fully coherent or fully relaxed material.

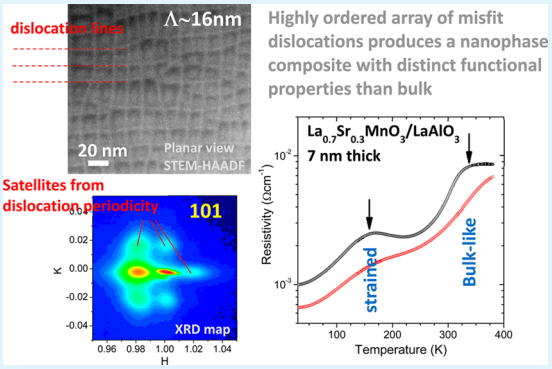

KEYWORDS: *strain relaxation, misfit dislocation arrangement, nanophase modulation, nanotemplate*

1. INTRODUCTION

Strain engineering in thin epitaxial films of transition metal oxides with perovskite structure has become an important field of study in the past decade because of the strong correlations between the subtle structure variations induced by the epitaxial growth on mismatched substrates and the electronic properties of oxide films, which have proven to render the film material very different functional properties to those of the equilibrium material.[1−4]

Lattice-mismatched heterostructures of perovskite oxides are also of interest because the regions surrounding the defects generated during the strain relief, typically misfit dislocations (MDs) or walls between crystal domains with different orientation, very often show a different structure and symmetry than the rest of the film material at the nanoscale.[5−7] This may offer a basis for fabrication of a variety of low-dimensional and mesoscopic systems in solid-state physics.[8−11]

In epitaxial growth on substrates with lattice mismatch, the film structure is submitted to an in-plane biaxial strain, either compressive or tensile depending on the mismatch with the substrate. The out-of-plane cell parameter is therefore expanded or compressed, as a result of the elastic response of the material. According to the classical model by Frank and van der Merwe[12] and Matthews-Blakeslee,[13] the films grow pseudomorphically with the substrate below a certain critical thickness. Above this thickness, the film usually releases the accumulated strain energy via plastic deformation, thus generating MDs, which progressively accommodate the strain toward the equilibrium bulk structure.[14]

At a local scale, the strain accommodation by a pure edge dislocation is uniaxial and was early described by the Peierls−

Received: March 8, 2016
Accepted: June 9, 2016
Published: June 9, 2016

DOI: 10.1021/acsami.6b02896
ACS Appl. Mater. Interfaces 2016, 8, 16823−16832

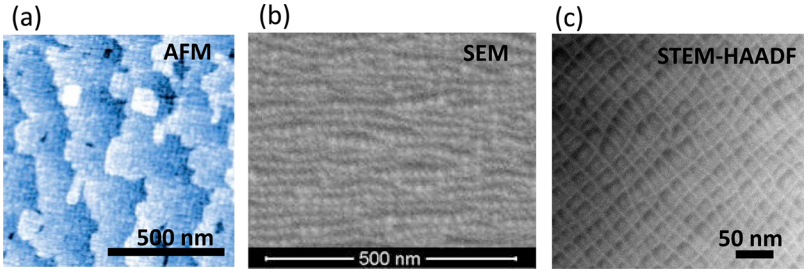

Figure 1. Planar view images of a 7 nm thick LSMO/LAO thin film with a well-developed MD pattern as observed by (a) AFM topography, (b) orientation contrast SEM, and (c) STEM taken at HAADF mode. In all cases, the image contrast defines parallel lines that correspond to the position of the MD cores parallel to [100] and [010] directions.

Nabarro model.[15] It follows the in-plane projection of the corresponding Burgers vector perpendicular to the dislocation line. Therefore, the biaxial strain in the films is necessarily accommodated by the formation of an array of MDs, as early observed by the concomitant formation of a cross-hatched surface morphology pattern in lattice-mismatched heterostructures of III−V semiconductors like GaAsP/GaAs,[16] which was further theoretically described by Speck and Pompe.[14] This is typically observed in thick films by means of optical or atomic force microscopy (AFM) but is difficult to trace in very thin films. The observation of MDs arrays has been more recently reported also in some perovskite oxide heterostructures such as in $SrRuO_3/SrTiO_3(100)$,[17] in buried $(Ca_{1-x}Sr_x)(Zr_{1-x}Ru_x)O_3/SrRuO_3/SrTiO_3(100)$,[18] in $La_{0.5}Ca_{0.5}MnO_3/SrTiO_3(100)$,[19] or in $BaTiO_3/SrTiO_3(100)$.[20]

In heterostructures that undergo strain relief by the formation of a high density of dislocations, they often arrange into highly ordered periodic patterns. This self-arrangement is induced by the repulsive forces generated in the interaction between MDs as well as their mobility along the interfaces, which depends on the elastic properties of the material and the deposition conditions. In an ideal case of a perfect periodical arrangement, it may provide a route to obtain the size uniformity needed for electronic applications such as in quantum dot arrays.[21] The dislocation pattern may also serve as a nanotemplate for the guided growth of 2D nanostructured materials, such as demonstrated in the preferential nucleation of Fe and Cu metal particles on strain-relieved Pt(111),[22] the growth of ZnSe nanowires and nanorod structures on GaAs,[23] as well as the growth of exotic nanomaterials seeded by screw dislocations.[24]

Understanding the formation and self-organization mechanism of such MD arrays in oxide perovskite materials is important for the fabrication of low-dimensional structures, thus providing an opportunity for the finding of novel physical phenomena. One perfect example is the recently reported condensation of two-dimensional oxide-interfacial charges into one-dimensional electron chains induced by the misfit-dislocation strain field in $(Nd_{0.35}Sr_{0.65})MnO_3/SrTiO_3$.[11]

This paper aims to investigate the progressive self-organization of the MD network occurring during the epitaxial growth of a heterostructure of complex oxide materials with perovskite structure submitted to a large biaxial compressive stress, exemplified by $La_{0.7}Sr_{0.3}MnO_3$ (LSMO) grown on $LaAlO_3$ (100) substrates (LAO). The strain modulation observed in ultrathin nanostructured films of LSMO material is correlated with the measured magnetotransport behavior.

2. EXPERIMENTAL METHODS

$La_{0.7}Sr_{0.3}MnO_3$ films with different thicknesses from 2.0−14.0 nm were deposited by magnetron sputtering under the same conditions and experimental setup as described in previous works.[25,26] $LaAlO_3(100)$ crystals (Crystec, GmbH) were used as substrates. The surface morphology along with the formation of MDs was examined by AFM (PicoSPM, Molecular Imaging, in tapping mode) and scanning electron microscopy (SEM; Quanta 200 FEG-ESEM, FEI). Detailed observations of the strain fields induced by the presence of the MDs were obtained by transmission electron microscopy (TEM) in HAADF (high angle annular dark field) mode as well as high-resolution TEM planar images (field emission gun Tecnai F20 S/TEM, FEI at 200 kV). High-resolution TEM images of film cross-section were obtained in a Cs-corrected microscope (F20 Tecnai, FEI). The overall film structure and the features induced by the arrangement of the MD network were analyzed by X-ray diffraction (XRD) making use of laboratory diffractometers (Panalytical X'Pert MRD, Rigaku SmartLab) for standard and in-plane diffraction geometry. The 2D X-ray reciprocal space mapping experiments were performed on beamline BM25 at the European Synchrotron Radiation Facility (ESRF), Grenoble, France. The 3D XRD reciprocal space maps were carried out by using synchrotron radiation at the KMC-2 beamline at Helmholtz-Zentrum Berlin (Bessy II). Resistivity of the films was measured as a function of temperature, from 10−380 K, in absence of magnetic field (H = 0 T) and in the presence of a magnetic field of H = 9T by using a physical properties measurement system (PPMS) from Quantum Design.

3. RESULTS AND DISCUSSION

All deposited films are continuous and show essentially flat morphology with single unit cell step terraces, as revealed by topography images obtained by AFM as depicted in Figure 1a, for the LSMO/LAO film of 7 nm thickness. A closer observation of the morphology of this film reveals the presence of a dense cross-hatched pattern following two perpendicular directions (corresponding to [100]/[010] main crystallographic directions), which form subtle ridges of less than one unit cell height. Figure 1b, shows the orientation contrast SEM image of the same 7 nm thick film. As in the previous AFM image, it shows a clear contrast forming a crossed pattern of parallel lines following [100]/[010] crystallographic directions. Because of the low film roughness and the absence of secondary phases, the corresponding SEM image shows only contrast related to crystallographic defects or strain fields. These lines presumably correspond to the presence of buried MDs at the interface between film and substrate generated because of the partial release of the misfit strain. A planar view scanning TEM (STEM) image of that film in HAADF is presented in Figure 1c. Again it shows a clear contrast forming lines running parallel to [100] and [010] main directions of the cubic primitive perovskite cell, in agreement with AFM and

DOI: 10.1021/acsami.6b02896
ACS Appl. Mater. Interfaces 2016, 8, 16823−16832

SEM observations. The bright lines in the HAADF image coincide with the position of the MDs core lines. The distance between dislocations is quite regular in the depicted area and spans from 20−30 nm.

High-resolution TEM observations of planar view and cross-section of the 7 nm LSMO/LAO film are shown in Figure 2a,b,

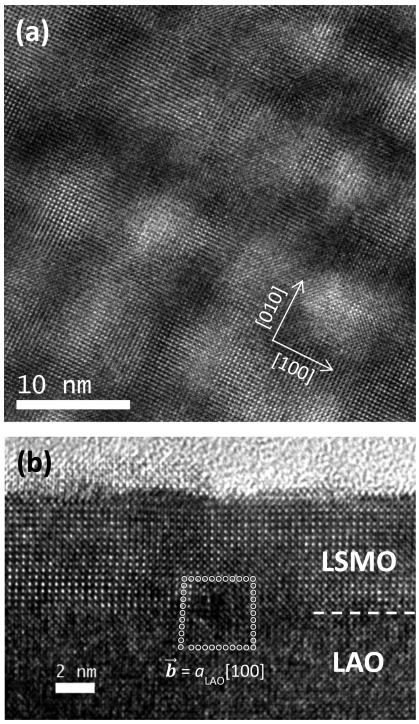

Figure 2. High-resolution TEM images of a (a) planar view and (b) cross-section of a 7 nm thick LSMO/LAO film. The cross-section shows a Burgers circuit around a MD core at the film−substrate interface with a Burgers vector $\mathbf{b} = a_{LAO}[100]$.

respectively. The planar view shows a high crystal quality with atomic column resolution. The dark and white contrast is related to the strain field caused by the MDs and shows a complex pattern already observed in the lower magnification image in Figure 1c. The cross-section image shows the presence of one MD core at the interface between film and substrate. The Burgers circuit around the MD core indicates a Burgers vector $\mathbf{b} = a_{LAO}[100]$ parallel to the interface with magnitude equal to one primitive unit cell of the LAO substrate, which is typical in perovskite oxides and was previously reported in LSMO/LAO.[27]

3.1. Evolution of MD Distribution with Film Thickness.

For a comparison of the MDs density evolution Figure 3a shows orientation-contrast SEM images of the LSMO films deposited on LAO substrates with different thicknesses from 2−14 nm. Orientation contrast-SEM (OC-SEM) images offer a direct method to reveal the presence of MDs pattern clearer than AFM and much simpler to prepare than TEM planar view specimens.

The thinnest film of 2 nm does not show any evidence of MD formation. However, the film with 3.5 nm thickness already shows a pattern of lines corresponding to MDs with different spacing. Films with larger thickness of 7 and 14 nm show a dense distribution of crossed MDs forming a regular grid. Therefore, from these images, it can be estimated that the critical thickness for the formation of MDs lies roughly between 2.0 and 3.5 nm, and the films progressively show a higher MD density with thickness.

To quantify the MDs distribution, Figure 4a shows histograms of their spacing obtained from a large number (about 190) of linear scans across the SEM images. They consist of a single mode Poisson distribution with different mean and standard deviation values as opposed to the bimodal distributions often observed in semiconductors (in the diluted MD dislocation regime) and related to the interaction between 60° dislocations with opposite in-plane component to form pure edge dislocations.[28] The film with 3.5 nm thickness shows a mean dislocation separation around 38 nm, which corresponds to a dislocation linear density of 2.6×10^5 cm^{-1}, while for the 7 and 14 nm thick samples, the mean separations were 25 and 16 nm, respectively (linear dislocation densities around 4.0×10^5 cm^{-1} and 6.2×10^5 cm^{-1}). For thicker films, the image of the dislocation gets blurred because of the limited penetration depth of the electrons, and it is difficult to accurately measure their separation by SEM. In a fully relaxed LSMO film (with cell parameter a_{LSMO}= 3.885 Å, and pseudocubic cell parameter a_{LAO} = 3.790 Å for the LAO substrate), a simple calculation gives a saturation MD density of 6.45×10^5 cm^{-1}, assuming a Burgers vector equal to one unit cell in the direction parallel to [100], $\mathbf{b} = a_{LAO}[100]$. This corresponds to one MD every 40 u.c. of the LSMO structure, that is, an average MD separation of 15.5 nm. The mean values of the experimental linear dislocation density progressively increase with thickness reaching almost full relaxation for the 14 nm thick sample. Figure 4b depicts that density as a function of the reciprocal film thickness. The dependence is roughly linear following the expression

$$\rho_{MD} = \rho_{relaxed}(1 - h_c/h) \quad (1)$$

above a critical thickness h_c before it reaches saturation at the maximum dislocation density for the fully relaxed films, consistent with Matthews and Blakeslee model.[13] The critical thickness value can be extrapolated from the $\rho_{MD} = 0$ intercept to be roughly 2.5 nm.

From thermodynamic equilibrium considerations, Matthews and Blakeslee derived a self-contained expression for the critical thickness, h_c:[29]

$$h_c = \frac{b}{4\pi f}\frac{(1 - \nu\cos^2\theta)}{(1 + \nu)\sin\theta\cos\phi}\ln\left(\frac{\alpha h_c}{b}\right) \quad (2)$$

where b is the modulus of the Burgers vector, f is the magnitude of the strain, ν is the Poisson ratio, and θ and ϕ are the angles between the Burgers vector and the dislocation line and the interface plane, respectively. The value of the dislocation core parameter, α, may vary between $\alpha = 1$ and $\alpha = 4$, and in practical cases, it is obtained from experimental data. As an estimate, in this case, we assume the value of $\alpha = 2.72$ first derived in the Matthews and Blakeslee theory.[29] The values of b = 3.885 Å (1 u.c.), mismatch $|f| = 0.024$, $\theta = 90°$, $\phi = 0°$, were taken for the present case of LSMO/LAO. The Poisson ratio was calculated from the experimental LSMO cell parameters of the fully strained 2.0 nm film measured by high-resolution XRD $2\theta/\omega$ scans (out-of-plane c = 3.985 Å; in-plane a = 3.790 Å). Assuming an equilibrium cell structure a = 3.885 Å, the corresponding strains are $\varepsilon_{//} = -0.0244$; $\varepsilon_{\perp} = +0.0257$, and the Poisson ratio calculated from the expression for biaxial strain $\varepsilon_{\parallel} = -(2\nu/1 - \nu)\varepsilon_{\perp}$[30] was $\nu = 0.32$. Therefore, a critical thickness

DOI: 10.1021/acsami.6b02896
ACS Appl. Mater. Interfaces 2016, 8, 16823−16832

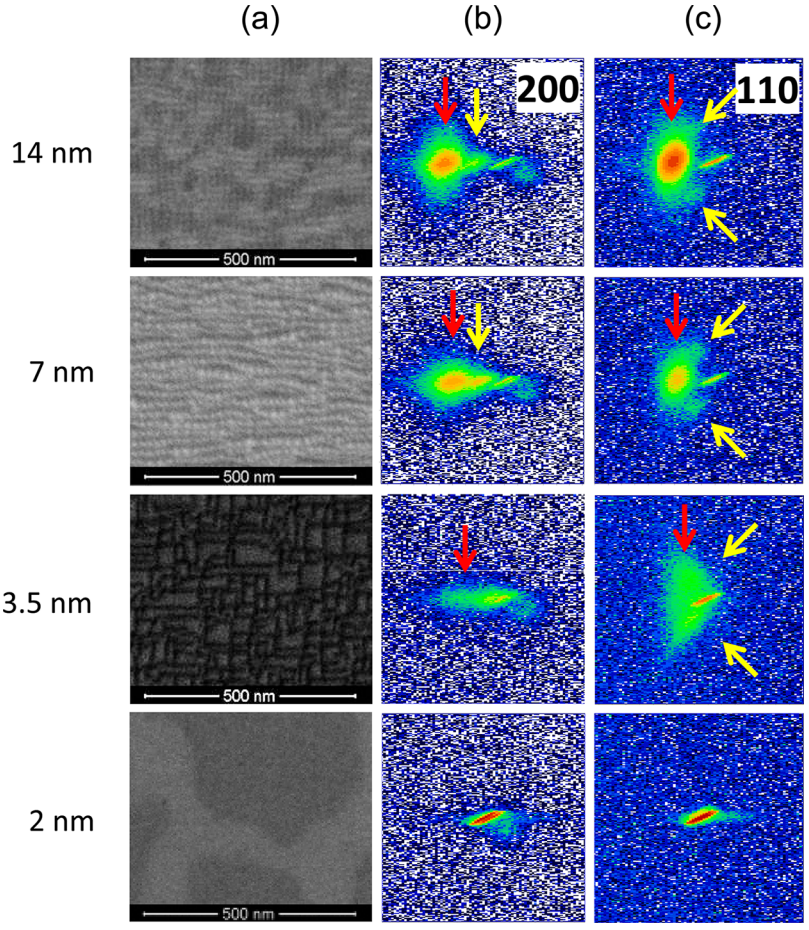

Figure 3. Chart shows details of LSMO films with different thicknesses from 2, 3.5, 7, and 14 nm. In columns (from left to right): (a) OC-SEM images of the same samples. The observed horizontal and vertical lines correspond to MDs running parallel to [100] and [010] crystallographic directions; in-plane XRD $2\theta-\phi$ area of (b) 200 and (c) 110 reflections of LSMO film and LAO substrate (obtained with CuKα radiation in laboratory diffractometer, at 0.5° incidence angle). The horizontal axis corresponds to 2θ angle and vertical axis to ϕ angle. These axes are approximately following the [100]/[010] directions for 200 reflection, and [110]/[−110] for 110. The angular range for both 2θ and ϕ scans was 4°.

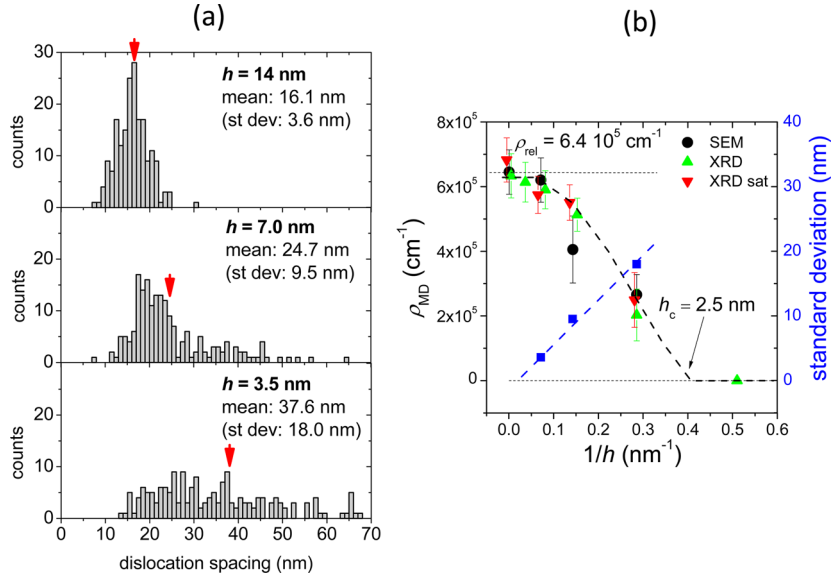

Figure 4. (a) Distribution histograms of the separation between consecutive MDs measured from the SEM images of the films of different thicknesses; (b) dependence of the linear dislocation density versus the reciprocal film thickness (as measured by SEM (black symbols) and XRD as estimated from the LSMO cell parameter value (green symbols) and from the satellite peak position (red symbols), along with the standard deviation of the distribution by SEM (blue symbols).

DOI: 10.1021/acsami.6b02896
ACS Appl. Mater. Interfaces 2016, 8, 16823−16832

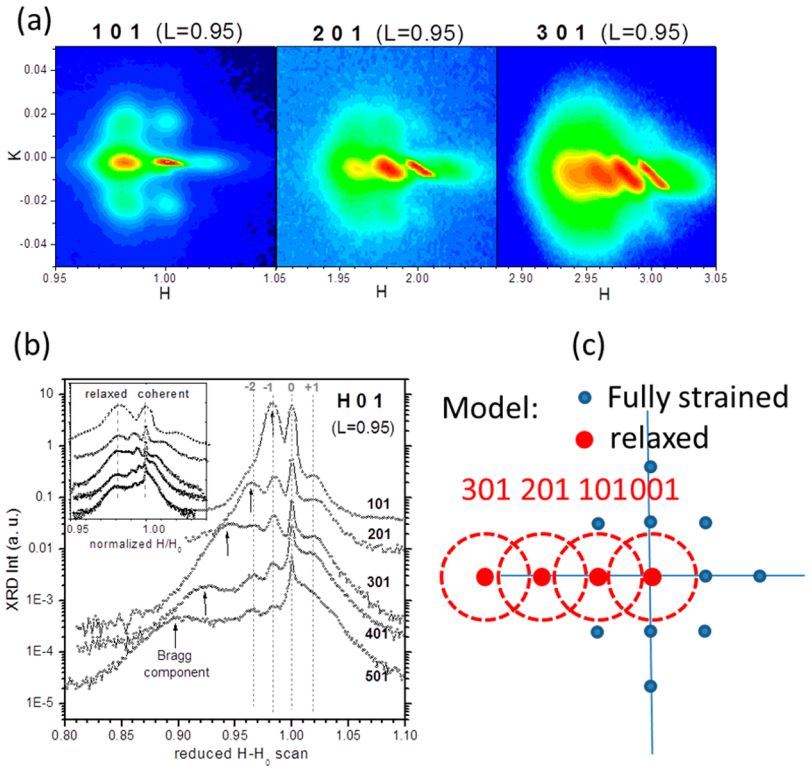

Figure 5. (a) *HK* reciprocal space maps of H 0 1 (H = 1, 2, and 3) reflections of the LSMO film with 7 nm thickness; (b) linear H scans of the different reflections H 0 1, from H = 1−5, the scans are shifted to coincide in the H position of the LAO substrate at H = 1 (the inset shows the same scans reduced dividing by H_0 along with (c) the corresponding model showing the overlap in the reciprocal space of fully strained and partially relaxed LSMO structures.

of h_c = 1.7 nm is obtained from eq 2, which is slightly below the experimental observation.

The standard deviation of the distribution of MD separation depicted in Figure 4a also varies with film thickness, being very wide for the 3.5 nm thick sample, which is about 18 nm. The standard deviation distribution becomes gradually reduced to about 9.5 and 3.6 nm for the 7 and 14 nm thick samples, respectively. The same graph in Figure 4b shows an almost linear dependence of the distribution standard deviations with the reciprocal thickness approaching to a zero value for the thicker films, which indicates the trend toward a perfect arrangement of the MD network. At the critical thickness, the distribution deviation extrapolates to very large values, which essentially indicate that at the very onset of the MD formation their distribution is flat with random separation distance between them. Upon the MD density increases, their strain fields interact, which progressively narrows their distribution until they self-arrange forming a highly ordered crossed network already at a film thickness of 7 nm.

It is also interesting to notice that in the 3.5 nm thick film, where the MD density is low and the self-arrangement is far from being complete, the MDs show also a wide distribution in length from long segments of several hundreds of nm to short dislocations of only a few tenths of nm, as evidenced in Figure 3a. Some MDs end within the film, although most of the MDs end when they meet another orthogonal MD line. This observation is consistent with the finding previously reported in SiGe and III−V semiconductors where the ends of the MDs turn into threading dislocations half loops emerging at the film surface.[31] In a regime with low density of MDs, the threading dislocations loops do not get annihilated and they persist in the film, their lateral diffusion being blocked by the strain field of some other crossing MD. Upon increasing the MD dislocation density, the threading dislocations have larger probability to overcome those barriers, eventually meeting another threading dislocations and annihilate each other, turning into longer sections of MD lines. In the 7 nm film, short length MDs are rare, and most of them extend for hundreds of nm, as observed in the SEM and TEM images in Figure 1b,c.

3.2. Structure Lateral Modulation. It is difficult to accurately measure the in-plane cell parameter for ultrathin films of only a few nm thickness by reciprocal space mapping because of their very weak signal and the overlap with the intense substrate peaks. Instead, the in-plane diffraction geometry (with grazing incidence and exit angles) allows for a qualitative insight into the in-plane cell parameter relaxation. This provides an alternative way to indirectly measure the MD density. Figure 3b,c show in-plane $2\theta-\phi$ area scans of 200 and 110 in-plane reflections, respectively. Any variation in the Bragg peak position along the horizontal 2θ-axis corresponds to a change in the in-plane cell parameter, while a variation in the vertical ϕ-axis most likely corresponds to some tilt in the structure. The 200 area scans of the 2.0 nm thick film show one single peak at around 2θ = 48° that corresponds to the same position expected for the LAO substrate. The slight elongation of the spot along [110] corresponds to an instrumental origin coming from the X-ray optics. The presence of one single peak indicates that the film in-plane cell parameters are coherent with those of the substrate, and therefore, the film is fully strained. Although this grazing angle geometry is intended to enhance the diffracted signal from the topmost part of the film, the penetration of the X-rays still gives a non-negligible overlap

DOI: 10.1021/acsami.6b02896
ACS Appl. Mater. Interfaces 2016, 8, 16823−16832

with the peak from the substrate for very thin films of a few nm. The same occurs for the corresponding 110 area scan where only one peak is observed. However, the 200 and 110 area scans of the 3.5 nm thick film show a considerable diffuse scattering at lower 2θ angles from the substrate peak, which point to an incipient relaxation of its in-plane cell parameter (red arrows). Interestingly, the diffuse scattering in the 110 area scan shows two different branches following [100] and [010] orthogonal directions (yellow arrows). This is an indication of the uniaxial relaxation character due to the presence of the crossed MDs.

The 200 and 110 area scans of the 7.0 and 14 nm thick films show a very sharp reflection corresponding to the LAO position (at larger 2θ angle, on the right of the scan) and a broader intense reflection (at lower 2θ angle, on the left) corresponding to the partially relaxed LSMO structure (red arrows). This peak position in the maps indicates that in-plane LSMO cell parameters relax equally along [100] and [010] directions, thus keeping a square basal a/b plane. The corresponding cell parameters were measured to be 3.865 and 3.877 Å for the 7.0 and 14 nm thick films, respectively. By taking these values, the numbers of unit cells between dislocations are calculated as N = 50 and 44, which correspond to distances of 19.5 and 17.0 nm, respectively. These values are in good agreement with those calculated from the SEM observations previously shown in Figure 3a and included in Figure 4b.

Along with the main Bragg peaks, these area scans show additional features, as indicated by yellow arrows. In the 200 area scans, between the substrate and film peak positions, there is a clear peak. This peak does not correspond to a Bragg peak. Instead, it corresponds to a first-order satellite peak coming from a lateral structure modulation within the film plane induced by the presence of the dislocation network. Those satellites are also observed in the in-plane XRD maps of the 110 reflection. They deviate from the [110] directions and split in phi angle (vertical axis in the scans) following the [100] and [010] directions, as in the thinner 3.5 nm film. This splitting corresponds to the previously mentioned modulation along the plane of the sample, along both [100] and [010] directions. The distance in the reciprocal space between the first satellite position and the zero order position (on the LAO position) was an indication of the modulation periodicity. For the 3.5, 7, and 14 nm thick LSMO films, the modulation period was calculated to be 40(±13), 18(±2), and 17(±2) nm, respectively, in good agreement with the separation between MDs. The corresponding MD linear densities for these data were also incorporated in Figure 4b.

A clearer view of the satellite pattern induced by the modulated structure is observed in the HK reciprocal space maps of the H01 reflections of the 7 nm thick film shown in Figure 5a for H = 1, 2, and 3. H, K, and L axes correspond to the [100], [010], and [001] directions, respectively (H, K, and L are expressed in reciprocal lattice units of the LAO substrate). These measurements were performed by using synchrotron radiation and were taken at the L = 0.95 position optimized for the LSMO film, slightly lower than the substrate position at L = 1 because in the relaxed LSMO structure, the c-axis parameter is larger than that for LAO. The sharp reflections at the (H = 1, K = 0) position along with (H = 2, K = 0) and (H = 3, K = 0) for in the 101, 201, and 301 maps, respectively, correspond to the LAO substrate overlapped with the fully strained LSMO component. The intense reflections at (H = 0.98, K = 0), (H = 1.96, K = 0), and (H = 2.94, K = 0) for the 101, 201, and 301 maps, respectively, correspond to the LSMO partially relaxed Bragg component. The rest of the peaks correspond to satellite reflections in positions ($H = H_0 \pm nd$, $K = 0 \pm md$) centered at the H_0 position of the fully coherent LSMO structure, being (n,m) the order of the satellite reflections along H and K directions in the map, respectively. The distance d between satellites along H and K shows a constant value of about 0.019 (in reciprocal space units) for all H 0 1 reflections, which is consistent with a square-shape in-plane modulation with periodicity $\Lambda \approx 20$ nm along both [100] and [010]. This is consistent with the presence of the crossed pattern of perfectly parallel MDs network. First-order satellites are clearly visible, while second- or third-order satellites are only visible in the proximity of the LSMO partially relaxed reflection.

Figure 5b shows the intensity profiles along linear H scans at K = 0 for the different H01 reflections (H = 1, 2, 3, 4, and 5). The scans have been translated so the position of the corresponding H01 LAO reflection coincides for all them at $H - H_0 = 1.0$. It is clear that satellite reflections (up to second order on the left part of the scan, indicated by the dashed vertical lines) keep the same separation in reciprocal space with respect to the central zero order ($H - H_0 = 1$) reflection, which is consistent with the in-plane modulation. The curves also show a broad component (indicated with arrows in the graph) progressively shifted to lower H values, from 101 to 501 reflections that corresponds to the Bragg component of the LSMO partially relaxed structure. The inset shows the same scans reduced by dividing by the corresponding H_0 value of the reflection. As expected, all the Bragg components show the same value at around H/H_0= 0.98 corresponding to an average in-plane cell parameter of 3.864 Å.

It is not surprising to notice that the partially relaxed LSMO component at the 101 and 201 reflections coincides with the position of $n = -1$ and $n = -2$ ($m = 0$) satellite reflections, respectively. In fact, for a fully relaxed LSMO structure, we might expect a dislocation distance Λ equal to $\Lambda = Na_{LSMO} = (N + 1)a_{LAO}$, where N is the number of unit cells of LSMO to exactly match $N + 1$ cells of LAO. Therefore, in the reciprocal space, the position of the nth order satellite will correspond to $Q_x^{\Lambda} = n(N + 1)^{-1}\ a_{LAO}{}^{-1}$. For a couple of HKL reflections of LSMO film and LAO substrate, their corresponding positions along [100]* direction in the reciprocal space are $Q_x^{LAO} = H\ a_{LAO}^{-1}$ and $Q_x^{LSMO} = H\ a_{LSMO}^{-1}$. If we calculate their separation in the reciprocal space, $\Delta Q_x^{LAO,LSMO} = (Q_x^{LAO} - Q_x^{LSMO}) = H(N + 1)^{-1}\ a_{LAO}^{-1}$. In this way, for a fully relaxed film, we should expect a perfect coincidence of the modulated structure when $H = n$. Since the 7 nm thick film is close to full relaxation, we observe such coincidence at n = 1 for the H = 1 (101) reflection, and n = 2 for the H = 2 (201) reflections.

The overlap of these reflections enhances the intensity of the satellites, along with those at $m = \pm 1$ (along [010]* direction). This is an indication of some degree of constructive interference between the scattered waveforms of both fully strained and fully relaxed LSMO components. As depicted in the sketch in Figure 5c, the pattern may be described as the overlap between (i) a fully strained LSMO contribution coherent with the LAO substrate, with the corresponding square shape satellite pattern generated by the MD periodicity (in blue), (ii) plus the partially relaxed LSMO component moving along H, depending on the H01 reflection (in red color). Since part of the partially relaxed structure is also modulated with the same periodicity, it is not surprising that it

DOI: 10.1021/acsami.6b02896
ACS Appl. Mater. Interfaces 2016, 8, 16823−16832

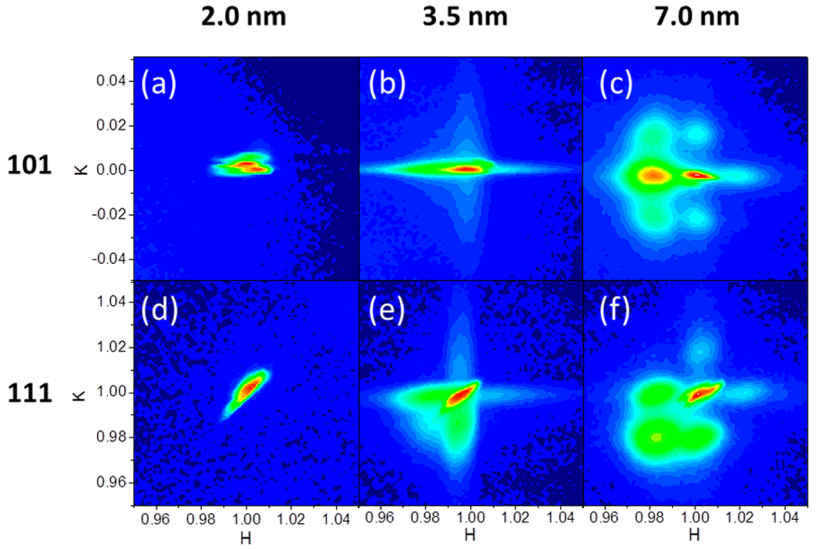

Figure 6. *HK* reciprocal space maps of the 101 and 111 reflections for the LSMO films with thickness (a, d) 2.1 nm, (b, e) 3.5 nm, and (c, f) 7.0 nm. Maps were positioned at $L = 0.95$ corresponding to the maximum of the LSMO contribution (*HKL* in LAO reciprocal lattice units).

reproduces the same satellite square pattern but centered in the LSMO reflection, with a certain coincidence in some satellite positions. In this way, the region around this last component (indicated as the dashed circle) enhances the intensity of the close satellite reflections.

To follow in more detail the progression of the MD generation and the degree of order of the strain pattern upon film thickness increase, reciprocal space *HK* maps of the 101 and 111 reflections were collected by using synchrotron radiation (at constant $L = 0.95$, as optimized for the LSMO signal), on the samples with 2.0, 3.5, and 7.0 nm thickness, as shown in Figure 6. Similarly to the in-plane 200 and 110 maps depicted in Figure 3b,c the 101 and 111 *HK* maps of the film with 2.0 nm, in Figure 6a,d show one single peak at ($H = 1$, $K = 0$) and ($H = 1$, $K = 1$), respectively, with no evidence of relaxation. These 101 and 111 reflections were optimized at $L = 0.95$ where film signal is maximum, thus minimizing the overlap with the very narrow LAO rod whose maximum, is at $L = 1$. The *HK* maps of the 3.5 nm thick film, shown in Figure 6b,e present diffuse scattering around the central position following [100] and [010] directions. Since the periodical arrangement of the dislocations is not yet established, the diffuse scattering associated with the linear defects shows broad branches. The substantial asymmetry of the map showing larger intensity tails at $H = 0.98$, $K = 0$, for the 101 map (left branch in Figure 6b), and $H = 0.98$, $K = 1$ and $H = 1$, $K = 0.98$ values, along the corresponding crossed branches in the 111 map (in bottom and left quadrant of Figure 6e), points to the uniaxial relaxation of the structure around each set of MDs. Still, there is a weak contribution to the biaxial relaxation visible in the 111 map along the [110] bisect direction at $H = 0.98$, $K = 0.98$. The very weak intensity of the branches at larger H and K values is the reason why they were not previously observed in the in-plane maps measured in the lab diffractometer with a conventional Cu$K\alpha$ tube source. The film with 7.0 nm thickness, in Figure 6c,f shows already a clear biaxially relaxed peak at $H = 0.98$, $K = 0$ for the 101 map, and $H = 0.98$, $K = 0.98$ for the 111 map. As in previous observations, the periodical arrangement of the crossed MDs defines clear first-order satellites around the central position. Again, the asymmetry between the intensities of the satellites is related to the degree of coherence between relaxed and strained LSMO structures, as explained in the model in Figure 5c. This makes particularly intense first-order satellites at ($H = 0.98$, $K = 1$) and (1, 0.98) positions for the 111 map as well as particularly intense second-order satellites in the 101 map at ($H = 0.98$, $K = \pm 0.02$) positions.

It is important to point out that the representation of the different *HK* maps at constant L value has some difficulties given the fact that the optimal value of L for maximizing the intensity of the reflection corresponding to the relaxed part of the LSMO structure is not exactly the same as for the LSMO structure coherent with the substrate. Since these structures are submitted to a different in-plane biaxial strain, they show different out-of-plane *c*-axis parameters. Similarly, the satellite reflections show a maximum intensity at different L positions. Therefore, it is more adequate to represent them in 3D. A collection of these 3D representations is shown in the Supporting Information.

3.3. Depth Distribution. Up to this point, we have described the LSMO/LAO films as a combination of a LSMO relaxed structure and a largely strained structure modulated by the presence of the MD network. It is very likely to expect that the modulated structure is in close proximity to the MD lines, and therefore close to the film−substrate interface, while the relaxed LSMO part may be at a certain distance from the dislocations close to the film surface. This difference along the depth of the sample was explored by grazing incidence in-plane diffraction by varying the incidence angle, and therefore the penetration depth of the X-rays. Figure 7a shows linear $2\theta - \chi$ scans around the 200 in-plane reflection of the 7 nm thick LSMO/LAO film for different ω incidence angles from 0.1−0.5°. The scans show the three components: relaxed LSMO at $2\theta - \chi = 47.0°$, fully strained LSMO with a possible overlap with LAO substrate at $2\theta - \chi = 48.0°$, and the intense first-order satellite of the modulated structure at $2\theta - \chi = 47.5°$. The overall intensity of the scan increases with the penetration depth. However, the relative intensities of the peaks vary with the incidence angle. Figure 7b depicts the relative intensity of the integrated area of the first order satellite peak compared to the relaxed LSMO reflection. The increase of this ratio with the incidence angle indicates that the relaxed LSMO part is closer to the film surface, while the modulated part is found deeper in

DOI: 10.1021/acsami.6b02896
ACS Appl. Mater. Interfaces 2016, 8, 16823−16832

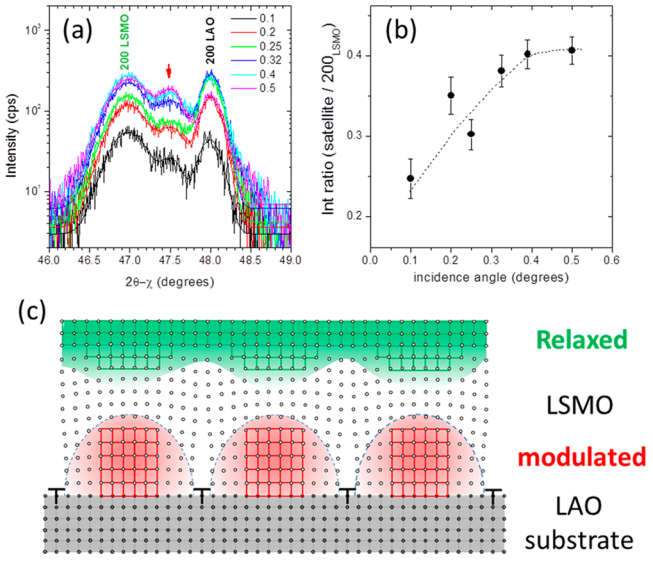

Figure 7. (a) In-plane diffraction $2\theta - \chi$ scans of the 200 reflection of the 7 nm thick LSMO/LAO film using different incidence ω angles from 0.1−0.5°. (b) Integrated intensity ratio of the satellite component versus the 200 LSMO Bragg reflection. (c) Model of the depth distribution of the outer relaxed LSMO and buried strained-modulated LSMO structure.

the film. The sketch in Figure 7c schematically represents the distribution of the two different phases. It is very likely that there is not a clear separation between these phases and there is a gradual change in strain between the top surface and the bottom interface of the film. The real situation may be even more complex if taken into account the strong strain field in the proximity of the MD cores. These may induce sudden changes in the sign of the linear strain but also in the shear strain, probably giving rise to more complex microstructure involving some local monoclinic distortions.

3.4. Influence on Film Functionality. The macroscopic observation of the planar resistivity in the films also evidences the formation of a distribution of two different phases. Figure 8 shows the resistivity of the films with different thicknesses from 2−14 nm at H = 0T (black) and H = 9T (red). The application of a magnetic field strongly enhances ferromagnetic correlations, and the associated decrease of resistance gives rise to the so-called Colossal magnetoresistance (CMR) effect. This response achieves its maximum close to the ferromagnetic (metallic) to paramagnetic (insulating) phase transition, that is, to the corresponding ferromagnetic transition temperature T_c. We observe from Figure 8 that there is a clear evolution of transport properties when film thickness is increased from an insulating-like behavior for ultrathin films to a ferromagnetic-metallic behavior typical of LSMO bulk for thicker films. Films with intermediate thickness, namely 3.5 and 7 nm films, exhibit more complex magnetotransport properties that, nevertheless, can be easily understood in terms of the distorted structure (average measured c/a cell parameter ratio), as reported in ref 27 and the presence of the dislocations network in these films. The thinnest film of 2.0 nm exhibits a highly resistive (insulating) behavior with no sign of ferromagnetic correlations in the range of temperatures available, thus suggesting a nonmagnetic character. In the absence of MDs, this film is in a coherently strained state with a very large c/a ratio of ∼1.06. In this situation, the extremely distorted octahedral environment is expected to promote selective orbital occupancy and electronic localization, thus leading to an antiferromagnetic-insulating behavior.[32] When thickness increases up to 3.5 and 7 nm, conductivity is enhanced, and magnetoresistive response appears as magnetic field promotes ferromagnetic correlations and electronic delocalization. Thus, it is reasonable to ascribe this behavior to the appearance of the dislocation network and the coexistence of a poor conducting phase in the distorted region between dislocations and a progressively increasing phase with reduced distortion and improved conductivity. In this way, the alternate arrangement of the dislocations leads to a complex conducting behavior of two competing phases with different resistances. At 3.5 nm, the relative extent of the insulating phase is large enough to block current paths at zero field (see Figure 8), but this blocking is overcome with the application of magnetic field. At 7 nm, both phases are of similar volume, which is manifested by the two distinct maxima in the resistance (around 150 and 320 K), each of them reflecting their corresponding transition temperature. For the thicker film (14 nm), bulk-like metallic behavior is recovered, and a single transition temperature is observed close to 330 K. In this case, the dominant undistorted phase governs the magnetotransport probably percolating through the whole sample since remnant distorted areas are confined to the interface region between film and substrate, as described in the sketch in Figure 7c. Therefore, in terms of their transport properties, there is a limited range of film thickness for the macroscopic manifestation of the nanophase mixture of phases.

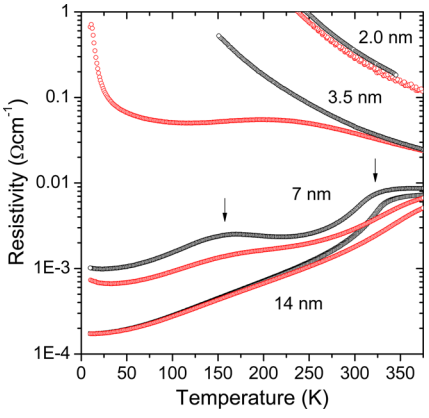

Figure 8. Resistivity versus temperature measured in thin LSMO/LAO films with different thickness at 0T (black) and 9T (red) applied magnetic field. The arrows indicate for the 7 nm thick film the maximum of magnetoresistance corresponding to the coexistence of low and high T_c phases.

3.5. Mechanism for MD Formation. Another striking observation of the LSMO films grown on LAO is that no twin formation was present in the whole range of thicknesses analyzed. This is clearly in contrast with previous observations of homogeneously twinned LSMO films with total absence of MDs when deposited on $SrTiO_3$ (STO) substrates at the same deposition conditions.[25,26] This different film microstructure on LAO substrates is explained in terms of the competition between the MDs and twin domain formation mechanisms.

MDs are generated during film growth at elevated temperatures depending on the film−substrate mismatch and film thickness. Little variations are expected to occur beyond that step once an equilibrium MD pattern is achieved. At 900 °C, close to the LSMO rhombohedral-to-cubic transformation, shear distortion is less than 0.05° as measured in LSMO/STO

DOI: 10.1021/acsami.6b02896
ACS Appl. Mater. Interfaces 2016, 8, 16823−16832

films in air.[26] Under these conditions, no twin domains are expected to form. Subsequently, the twin domains nucleate during the cooling step upon release of the progressively increasing shear stress of the LSMO rhombohedral film structure. The distorted structure nuclei grow until they meet another transformed domain. In LSMO films with no MDs when grown on STO, the rhombohedral domains compete with each other and arrange forming a homogeneous distribution of striped twin domains, thus achieving a long-range order depending on the crystal quality of the original crystal matrix. In LSMO/STO, striped twin domains were observed from early stages of the growth (above 2.0 nm thickness). However, in the LSMO films on LAO, since a high density of MDs is already formed at high temperature, the growth front of the transformed nuclei is most likely confined by the strain field originated by the buried MDs, particularly in ultrathin films. Therefore, it is blocking the long-range order of the twin domains and no striped microstructure is achieved. Only sufficiently thick films may transform generating a distribution of twin domains once the influence of the buried MDs is minimized.

There are several competing mechanisms that cause LSMO films on STO to not show any evidence of MD formation, even at film thicknesses as large as several hundreds of nanometres (despite of the critical thickness value $h_c \approx 5$ nm calculated from eq 2 assuming a + 0.7% tensile strain of LSMO on STO). This is evidently in contrast with the early formation of MDs on LAO. In a previous work, it was described that in LSMO/STO, the tensile strain is accommodated by an enrichment of the Mn^{3+} oxidation state at the interface, thus enlarging the equilibrium cell volume.[25] In the absence of a La/Sr composition segregation, the charge is compensated by the generation of oxygen vacancies. This reduces the film−substrate mismatch, which avoids the formation of MDs. However, this mechanism is precluded for the −2.4% compressive strain on LAO because the necessary cell volume reduction, which could be induced by the enhancement of Mn^{4+} oxidation state, cannot be compensated with an oxygen excess. Moreover, it cannot be ruled out that the absence of MDs in the LSMO films under tensile strain may be also related to an enhancement in the energy barrier for their nucleation and diffusion in comparison to films under compressive biaxial stress. This is not surprising and was already described in early studies. Generally, in semiconducting materials, and to a lower extent in metal heterostructures, there were observed some discrepancies on the critical thickness between the standard models and the experimental density of dislocations, which were attributed to non-negligible energies for the MD nucleation at the free surface of the film, as well as for their propagation toward the film−substrate interface.[29] The dislocation nucleation energy depends largely in the sign of the stress, and the critical thickness for MD nucleation is generally smaller for compression than under tension.[33] The fact that the experimental critical thickness obtained in these series of LSMO/LAO samples, $h_c = 2.5$ nm, does not deviate too much from that calculated from a thermodynamic equilibrium model of 1.7 nm is an indication that under compression there are not substantial barriers for MD nucleation and propagation, as opposed to the growth LSMO under tension.

4. CONCLUSIONS

In summary, we have observed that LSMO/LAO under large compressive strain of −2.4% starts relaxing forming MDs from a critical thickness of about 2.5 nm. Progressively, the MDs density increases, which follows the expected linear dependence with the reciprocal thickness. At high enough linear densities, above 5×10^5 cm^{-1}, they self-arrange to form a periodic crossed network of edge dislocations with a very narrow distribution of distances. The highly ordered defect structure produces a lateral superperiodicity in the films that can be readily analyzed by XRD in perfect correlation with the direct observation of the MD lines by SEM and TEM. The presence of such high density of MDs blocks the formation of long striped twin domains. It is very likely that at a local scale the material transforms to the rhombohedral equilibrium structure. However, for the very thin films analyzed in this work, the domains are constrained within the nanoscale square regions flanked by crossed MDs, and twin walls were not observed. Within these small regions, the concurrence of domains with uniaxial relaxation in perpendicular directions very likely induces a complex pattern of cell distortions as exemplified in the strain contrast pattern of the planar view images in Figures 1c and 2a. The accurate description of this pattern falls beyond the scope of this study and is intended for further work, in correlation with high resolution planar view TEM images. The highly ordered distribution of nanophases with a different cell distortion results in the simultaneous appearance of low and high T_c transition temperatures in the resistivity curves, but only in a limited range of film thickness. The achievement of a control over the defect arrangement along with the confinement of the rhombohedral-cubic transformation at the nanoscale may produce a combination of metastable phases with unique physical properties as well as serve as a template for subsequent growth of heterostructures with lateral periodicity.

■ ASSOCIATED CONTENT

Supporting Information

The Supporting Information is available free of charge on the ACS Publications website at DOI: 10.1021/acsami.6b02896.

3D representation of reciprocal space maps of 002 symmetric, as well as 301 and 113 asymmetric reflections for different film thickness measured at KMC-2 beamline at HZB (Bessy II) (PDF)

Video of 3D representation of reciprocal space map of the 113 reflection (AVI)

■ AUTHOR INFORMATION

Corresponding Author

*E-mail: jose.santiso@icn2.cat. Phone: +34 93 7373634.

Author Contributions

The manuscript was written through contributions of all authors. All authors have given approval to the final version of the manuscript.

Notes

The authors declare no competing financial interest.

■ ACKNOWLEDGMENTS

This research was funded by the Spanish MINECO (projects: MAT2011-29081-C02, MAT2012-33207, and MAT2013-47869-C4-1-P, Consolider-Ingenio CSD2008-00023) and the European Union Horizon 2020 research and innovation programme under the Marie Sklodowska-Curie Grant Agreement No. 645658. We also acknowledge financial aid from the Generalitat de Catalunya (2014 SGR 501 and 2014 SGR 1216).

DOI: 10.1021/acsami.6b02896
ACS Appl. Mater. Interfaces 2016, 8, 16823−16832

J.S. thanks the support of Ministry of Education and Science through program "Salvador de Madariaga" for a grant (ref: PRX14/00297) to perform a stay at MIT. Z.K. is grateful for the support from the Ministry of Education, Science, and Technological Development of the Republic of Serbia through Project No. III45018. Q.L. and B.Y. thank the National Science Foundation for support through the MIT Center of Materials Science and Engineering MRSEC under Grant No. DMR-1419807. This work made use of the Shared Experimental Facilities supported in part by the MRSEC Program of the National Science Foundation under Award No. DMR-1419807. We thank Dr. Belén Ballesteros (ICN2, Barcelona) and Prof. Marie-Jo Casanova (CEMES, Toulouse) for their assistance with TEM experiments. We are grateful to J. Rubio-Zuazo and the ESRF for providing assistance in using beamline BM25. We also thank HZB for the allocation of synchrotron radiation beamtime at Bessy.

REFERENCES

(1) Schlom, D. G.; Chen, L. Q.; Eom, C. B.; Rabe, K. M.; Streiffer, S. K.; Triscone, J. M. Strain Tuning of Ferroelectric Thin Films. *Annu. Rev. Mater. Res.* **2007**, *37*, 589−626.

(2) Jang, H. W.; Baek, S. H.; Ortiz, D.; Folkman, C. M.; Das, R. R.; Chu, Y. H.; Shafer, P.; Zhang, J. X.; Choudhury, S.; Vaithyanathan, V.; Chen, Y. B.; Felker, D. A.; Biegalski, M. D.; Rzchowski, M. S.; Pan, X. Q.; Schlom, D. G.; Chen, L. Q.; Ramesh, R.; Eom, C. B. Strain-Induced Polarization Rotation in Epitaxial (001) $BiFeO_3$ Thin Films. *Phys. Rev. Lett.* **2008**, *101*, 107602.

(3) Bozovic, I.; Logvenov, G.; Belca, I.; Narimbetov, B.; Sveklo, I. Epitaxial Strain and Superconductivity in $La_{2-x}Sr_xCuO_4$ Thin Films. *Phys. Rev. Lett.* **2002**, *89*, 107001.

(4) Schlom, D. G.; Chen, L. Q.; Pan, X.; Schmehl, A.; Zurbuchen, M. A. (2008). A Thin Film Approach to Engineering Functionality into Oxides. *J. Am. Ceram. Soc.* **2008**, *91*, 2429−2454.

(5) Catalan, G.; Seidel, J.; Ramesh, R.; Scott, J. F. (2012). Domain Wall Nanoelectronics. *Rev. Mod. Phys.* **2012**, *84*, 119.

(6) Farokhipoor, S.; Magén, C.; Venkatesan, S.; Íñiguez, J.; Daumont, C. J.; Rubi, D.; Snoeck, E.; Mostovoy, M.; de Graaf, C.; Müller, A.; Döblinger, M.; Scheu, C.; Noheda, B. Artificial Chemical and Magnetic Structure at the Domain Walls of an Epitaxial Oxide. *Nature* **2014**, *515*, 379−383.

(7) Arredondo, M.; Ramasse, Q. M.; Weyland, M.; Mahjoub, R.; Vrejoiu, I.; Hesse, D.; Browning, N. D.; Alexe, M.; Munroe, P.; Nagarajan, V. Direct Evidence for Cation Non-Stoichiometry and Cottrell Atmospheres Around Dislocation Cores in Functional Oxide Interfaces. *Adv. Mater.* **2010**, *22*, 2430−2434.

(8) Chu, M. W.; Szafraniak, I.; Scholz, R.; Harnagea, C.; Hesse, D.; Alexe, M.; Gösele, U. Impact of Misfit Dislocations on the Polarization Instability of Epitaxial Nanostructured Ferroelectric Perovskites. *Nat. Mater.* **2004**, *3*, 87−90.

(9) Nagarajan, V.; Jia, C. L.; Kohlstedt, H.; Waser, R.; Misirlioglu, I. B.; Alpay, S. P.; Ramesh, R. Misfit Dislocations in Nanoscale Ferroelectric Heterostructures. *Appl. Phys. Lett.* **2005**, *86*, 192910.

(10) Lubk, A.; Rossell, M. D.; Seidel, J.; Chu, Y. H.; Ramesh, R.; Hÿtch, M. J.; Snoeck, E. Electromechanical Coupling among Edge Dislocations, Domain Walls, and Nanodomains in $BiFeO_3$ Revealed by Unit-Cell-Wise Strain and Polarization Maps. *Nano Lett.* **2013**, *13*, 1410−1415.

(11) Chang, C. P.; Chu, M. W.; Jeng, H. T.; Cheng, S. L.; Lin, J. G.; Yang, J. R.; Chen, C. H. Condensation of Two-Dimensional Oxide-Interfacial Charges into One-Dimensional Electron Chains by the Misfit-Dislocation Strain Field. *Nat. Commun.* **2014**, *5*, 3522.

(12) Frank, F. C.; Van der Merwe, J. H. One-Dimensional Dislocations. II. Misfitting Monolayers and Oriented Overgrowth. *Proc. R. Soc. London, Ser. A* **1949**, *198*, 216−225.

(13) Matthews, J. W.; Blakeslee, A. E. Defects in epitaxial multilayers: II. Dislocation Pile-ups, Threading Dislocations, Slip Lines and Cracks. *J. Cryst. Growth* **1975**, *29*, 273−280.

(14) Speck, J. S.; Pompe, W. Domain Configurations Due to Multiple Misfit Relaxation Mechanisms in Epitaxial Ferroelectric Thin Films. I. Theory. *J. Appl. Phys.* **1994**, *76*, 466−476.

(15) Nabarro, F. R. N. Dislocations in a Simple Cubic Lattice. *Proc. Phys. Soc.* **1947**, *59*, 256.

(16) Kishinû, S.; Ogirima, M.; Kurata, K. A Cross-Hatch Pattern in $GaAs_{1-x}P_x$ Epitaxially Grown on GaAs Substrate. *J. Electrochem. Soc.* **1972**, *119*, 617−622.

(17) Sánchez, F.; Garcıa-Cuenca, M. V.; Ferrater, C.; Varela, M.; Herranz, G.; Martınez, B.; Fontcuberta, J. Transition from Three-to Two-Dimensional Growth in Strained $SrRuO_3$ Films on $SrTiO_3$ (001). *Appl. Phys. Lett.* **2003**, *83*, 902.

(18) Kim, S. G.; Wang, Y.; Chen, I.-W. Strain Relaxation in Buried $SrRuO_3$ Layer in $(Ca_{1-x}Sr_x)$ $(Zr_{1-x}Ru_x)O_3/SrRuO_3/SrTiO_3$. *Appl. Phys. Lett.* **2006**, *89*, 031905.

(19) Wang, Z. H.; Lebedev, O. I.; Van Tendeloo, G.; Cristiani, G.; Habermeier, H. U. Crosshatching on $La_{0.5}Ca_{0.5}MnO_3$ Ultrathin Films Epitaxially Grown on $SrTiO_3$(100). *Phys. Rev. B: Condens. Matter Mater. Phys.* **2008**, *77*, 115330.

(20) Sun, H. P.; Tian, W.; Pan, X. Q.; Haeni, J. H.; Schlom, D. G. Evolution of Dislocation Arrays in Epitaxial $BaTiO_3$ Thin Films Grown on (100)$SrTiO_3$. *Appl. Phys. Lett.* **2004**, *84*, 3298−3300.

(21) Tersoff, J.; Teichert, C.; Lagally, M. G. Self-Organization in Growth of Quantum Dot Superlattices. *Phys. Rev. Lett.* **1996**, *76*, 1675.

(22) Kern, K.; Brune, H.; Giovannini, M.; Bromann, K. Self-Organized Growth of Nanostructure Arrays on Strain-Relief Patterns. *Nature* **1998**, *394*, 451−453.

(23) Zhang, X.; Liu, Z.; Li, Q.; Leung, Y.; Ip, K.; Hark, S. Routes to Grow Well-Aligned Arrays of ZnSe Nanowires and Nanorods. *Adv. Mater.* **2005**, *17*, 1405−1410.

(24) Meng, F.; Morin, S. A.; Forticaux, A.; Jin, S. Screw Dislocation Driven Growth of Nanomaterials. *Acc. Chem. Res.* **2013**, *46*, 1616−1626.

(25) Sandiumenge, F.; Santiso, J.; Balcells, L.; Konstantinovic, Z.; Roqueta, J.; Pomar, A.; Espinós, J. P.; Martínez, B. Competing Misfit Relaxation Mechanisms in Epitaxial Correlated Oxides. *Phys. Rev. Lett.* **2013**, *110*, 107206.

(26) Santiso, J.; Balcells, L.; Konstantinovic, Z.; Roqueta, J.; Ferrer, P.; Pomar, A.; Martínez, B.; Sandiumenge, F. Thickness Evolution of the Twin Structure and Shear Strain in LSMO films. *CrystEngComm* **2013**, *15*, 3908−3918.

(27) Sandiumenge, F.; Bagués, N.; Santiso, J.; Paradinas, M.; Pomar, A.; Konstantinovic, Z.; Ocal, C.; Balcells, Ll.; Casanove, M.-J.; Martínez, B. Misfit Dislocation Guided Topographic and Conduction Patterning in Complex Oxide Epitaxial Thin Films. *Adv. Mater. Interfaces* **2016**, DOI: 10.1002/admi.201600106.

(28) MacPherson, G.; Goodhew, P. J.; Beanland, R. A Model for the Distribution of Misfit Dislocations Near Epitaxial Layer Interfaces. *Philos. Mag. A* **1995**, *72*, 1531−1545.

(29) Matthews, J. W.; Blakeslee, A. E. Defects in Epitaxial Multilayers: I. Misfit Dislocations. *J. Cryst. Growth* **1974**, *27*, 118−125.

(30) Ohring, M. *Materials Science of Thin Films*, 2nd ed.; Academic Press: New York, 2002.

(31) Freund, L. B. Dislocation Mechanisms of Relaxation in Strained Epitaxial Films. *MRS Bull.* **1992**, *17*, 52−60.

(32) Fang, Z.; Solovyev, I. V.; Terakura, K. Phase Diagram of Tetragonal Manganites. *Phys. Rev. Lett.* **2000**, *84*, 3169.

(33) Dong, L.; Schnitker, J.; Smith, R. W.; Srolovitz, D. J. Stress Relaxation and Misfit Dislocation Nucleation in the Growth of Misfitting Films: A Molecular Dynamics Simulation Study. *J. Appl. Phys.* **1998**, *83*, 217.

DOI: 10.1021/acsami.6b02896
ACS Appl. Mater. Interfaces 2016, 8, 16823−16832